Author Manuscript

Author Manuscript

Author Manuscript

Author Manuscript

HHS Public Access

Author manuscript

Nanomedicine. Author manuscript; available in PMC 2019 April 01.

Published in final edited form as:

Nanomedicine. 2018 April ; 14(3): 769–780. doi:10.1016/j.nano.2017.12.015.

Indocyanine green loaded hyaluronan-derived nanoparticles for fluorescence-enhanced surgical imaging of pancreatic cancer

Bowen Qi, MS[1], **Ayrianne J. Crawford, BS**[2], **Nicholas E. Wojtynek, BS**[2], **Megan B. Holmes, BS**[1], **Joshua J. Souchek, PhD**[1], **Graca Almeida-Porada, MD, PhD**[3], **Quan P. Ly, MD**[4,5], **Samuel M. Cohen, MD, PhD**[6,7], **Michael A. Hollingsworth, PhD**[2,5], and **Aaron M. Mohs, PhD**[1,5,8,*]

[1]Department of Pharmaceutical Sciences, University of Nebraska Medical Center, Omaha, Nebraska 68198, United States

[2]Eppley Institute for Research in Cancer and Allied Diseases, University of Nebraska Medical Center, Omaha, Nebraska 68198, United States

[3]Wake Forest Institute for Regenerative Medicine, Wake Forest University Health Sciences, Winston-Salem, North Carolina 27157, United States

[4]Department of Surgery, University of Nebraska Medical Center, Omaha, Nebraska 68198, United States

[5]Fred and Pamela Buffett Cancer Center, University of Nebraska Medical Center, Omaha, Nebraska 68198, United States

[6]Department of Pathology and Microbiology, University of Nebraska Medical Center, Omaha, Nebraska 68198, United States

[7]Havlik-Wall Professor of Oncology, University of Nebraska Medical Center, Omaha, Nebraska 68198, United States

[8]Department of Biochemistry and Molecular Biology, University of Nebraska Medical Center, Omaha, Nebraska 68198, United States

Abstract

Pancreatic ductal adenocarcinoma is highly lethal and surgical resection is the only potential curative treatment for the disease. In this study, hyaluronic acid derived nanoparticles with physico-chemically entrapped indocyanine green, termed NanoICG, were utilized for intraoperative near infrared fluorescence detection of pancreatic cancer. NanoICG was not cytotoxic to healthy pancreatic epithelial cells and did not induce chemotaxis or phagocytosis, it

[*]Correspondence to: Aaron M. Mohs, Ph.D., Department of Pharmaceutical Sciences, University of Nebraska Medical Center, 5-12315 Scott Research Tower, Fred and Pamela Buffett Cancer Center, Omaha, NE 68198-6858, aaron.mohs@unmc.edu.

AMM is a co-inventor of image-guided surgery technology that is licensed to Spectropath, Inc. (Atlanta, GA). The work described here was presented in part at the 4th Biopharmaceutical Research & Development Symposium (UNMC) from Sep 7–8, 2017 and World Molecular Imaging Congress (Philadelphia, PA) from Sep 13–16, 2017.

Publisher's Disclaimer: This is a PDF file of an unedited manuscript that has been accepted for publication. As a service to our customers we are providing this early version of the manuscript. The manuscript will undergo copyediting, typesetting, and review of the resulting proof before it is published in its final citable form. Please note that during the production process errors may be discovered which could affect the content, and all legal disclaimers that apply to the journal pertain.

Author Manuscript Author Manuscript Author Manuscript Author Manuscript

accumulated significantly within the pancreas in an orthotopic pancreatic ductal adenocarcinoma model, and demonstrated contrast-enhancement for pancreatic lesions relative to non-diseased portions of the pancreas. Fluorescence microscopy showed higher fluorescence intensity in pancreatic lesions and splenic metastases due to NanoICG compared to ICG alone. The *in vivo* safety profile of NanoICG, including, biochemical, hematological, and pathological analysis of NanoICG-treated healthy mice, indicates negligible toxicity. These results suggest that NanoICG is a promising contrast agent for intraoperative detection of pancreatic tumors.

Graphical abstract

A hyaluronic acid nanoformulation of indocyanine green (NanoICG) contrast-enhanced pancreatic ductal adenocarcinoma (PDAC) during surgical navigation and ex vivo analysis. The enhancement of the syngeneic, orthotopic PDAC was significantly higher compared to adjacent healthy pancreas and compared to tumor enhanced by ICG alone.

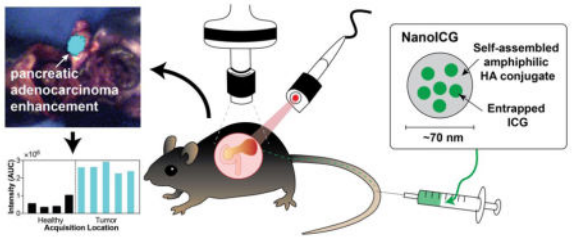

Keywords

Pancreatic ductal adenocarcinoma; hyaluronic acid; indocyanine green; fluorescence image-guided surgery; splenic metastasis

Introduction

Pancreatic ductal adenocarcinoma (PDAC) is highly lethal due to the advanced stage at diagnosis, with a median overall survival of 15 months and 5-year survival rate of 13%.[1] Detection and surgical resection at earlier stages increases 5-year survival to 31.7 ± 3.6 months.[2] Enhanced contrast can aid surgeons to confirm suspected pancreatic masses and elucidate positive margins.[3] Therefore, improved tumor imaging techniques that can better recognize cancerous lesions are essential to improve complete removal of PDAC and subsequent survival. At present, tumor localization and assessment of disease extension are made with visual inspection and palpation,[4] which can lead to incomplete resection or unnecessary removal of healthy tissue. Using tumor-specific contrast agents, image-guided surgery facilitates real-time, intraoperative, and visual identification of pancreatic tumors with improved discrimination of malignant and normal tissue.[5]

Clinically available preoperative imaging modalities, such as computed tomography (CT), magnetic resonance imaging (MRI), and positron emission tomography (PET), are critical to surgical planning. However, translating these results to the operating room is difficult due to altered body positioning, tissue manipulation, and lack of sensitivity to detect microscopic lesions.[6] Therefore, an intraoperative imaging technique with high accuracy and sensitivity

Author Manuscript Author Manuscript Author Manuscript Author Manuscript

is needed to fill the gap between preoperative and intraoperative reality. Current techniques that are used to assess pancreatic tumor extension intraoperatively, such as ultrasonography (US) and intraoperative frozen-section analysis (IFSC), have limitations. Substantial experience is required to generate and interpret useful US images during pancreatic cancer surgery.[6] Although IFSC is useful in ensuring negative margins, it has a negative predictive value of 50% for examining pancreatic lesions that could result in poor histological diagnosis and determination of resectability.[7]

Fluorescence imaging offers a potential method to detect pancreatic cancer intraoperatively to maximize malignant tissue resection. Fluorescence image-guided surgery (FIGS) can detect fluorescent contrast agents with high sensitivity and spatial resolution, which minimizes contrast agent dose and allows real-time determination of tissue status.[8,9] For example, AlexaFluor488 conjugated CA19-9 antibody was used to detect primary tumor and splenic and liver metastases of pancreatic cancer during surgical navigation.[10] Furthermore, near infrared (NIR) FIGS can minimize interference caused by tissue autofluorescence, scattering, and absorption, allowing relatively deep detection of contrast agent.[11,12] Metidi *et al.* demonstrated usage of MMP-2 and MMP-9 cleavable peptides conjugated Cy7 for accurate labeling of pancreatic tumors with FIGS in an orthotopic human xenograft mouse model, this resulted in a lower metastatic burden and decreased distant recurrence compared with resection surgery under standard bright light.[13] Yang *et al.* used magnetic iron oxide nanoparticles modified with Cy5.5 conjugated ATF (amino-terminal fragment) of uPA (urokinase plasminogen activator) for surgical detection of pancreatic cancer lesions.[14] Combined, fluorophore conjugated monoclonal antibody probes were used in animal models of pancreatic cancer with improved specificity, however, their efficacy was limited by naturally existing cellular targets that are often heterogeneously expressed in tumors and possibly in low abundance compared to background signals.[15] Therefore, a more generally applicable NIR fluorescent (NIRF) probe could have potential for NIR FIGS for reducing PDAC tumor burden.

Here, we report the use of a hyaluronic acid (HA) nanoformulation of ICG, termed NanoICG, for tumor detection in an orthotopic, syngeneic model of pancreatic cancer. ICG is an FDA-approved NIR fluorophore that can be detected through up to 8 mm of tissue.[16–18] On the other hand, HA is a major component of extracellular matrix that participates in cell proliferation, wound healing, and cancer metastasis.[19] With modifiable chemical groups such as carboxylate, N-acetylglucosamine, hydroxyl, and acetyl moieties, HA is readily available for chemical conjugation.[20,21] Recently, we reported that NanoICG increased NIR tumor signal by 2.28- and 2.25-fold compared to ICG in MDA-MB-231 xenograft[22] and 4T1 syngeneic orthotopic[17] breast tumor models, demonstrating potential for sensitive tumor detection. In this study, NanoICG was compared to ICG as a NIR FIGS contrast agent for the intraoperative detection and contrast-enhancement of pancreatic cancer in a syngeneic, orthotopic model. Results from *in vitro* and *in vivo* studies indicated that NanoICG is a safe contrast agent that can potentially be used in pancreatic tumor detection and surgical resection.

Author Manuscript Author Manuscript Author Manuscript Author Manuscript

Methods

Materials

ICG, luminol, and zymosan A were purchased from Sigma-Aldrich (St. Louis, MO). 10 kDa – 20 kDa sodium hyaluronate was purchased from Lifecore Biomedical (Chaska, MN). HPNE cell line was provided by Dr. Michel J. Ouellette from University of Nebraska Medical Center, while the KPC cell line was shared by Dr. Hollingsworth. HL-60 cells were purchased from ATCC (Manassas, VA). HPNE cells were grown in 70% DMEM with 25% medium M3, 5% FBS, 20 ng/mL human recombinant EGF, 1% penicillin/streptomycin; KPC cells were grown in DMEM with 10% FBS and 1% penicillin/streptomycin, HL-60 was maintained in IMDM with 20% FBS. Cell counting kit-8 (CCK-8) was purchased from Dojindo Molecular Technologies Inc. (Rockville, MD). Calcein AM was purchased from Invitrogen (Carlsbad, CA). 10-week-old female C57BL/6J mice were purchased from Jackson Laboratories (Bar Harbor, ME). 5.0 chromic gut and 5.0 nylon surgical sutures were purchased from Johnson & Johnson (Somerville, NJ). Comprehensive diagnostic profile reagent rotor was purchased from Abaxis (Union City, CA). All the other chemicals were purchased and used at analytical grade.

Preparation and Characterization of NanoICG

The synthesis of amphiphilic HA-aminopropyl-1-pyrenebutanamide (HA-PBA), preparation of NanoICG from the entrapment of ICG during HA-PBA self-assembly, and quantification of ICG in NanoICG were performed based on the literature.[17,22] The mean hydrodynamic diameter and zeta-potential of NanoICG was determined using a Zetasizer Nano instrument (Malvern, Worcestershire, UK). NanoICG was prepared at 0.34 mg/mL for size determination and 0.06 mg/mL for the determination of UV-visible absorption and fluorescence emission. An Evolution 220 spectrophotometer (Thermo Fisher Scientific, Madison, WI, USA) was used for scanning absorbance spectra (600–900 nm) and a FluoroMax-4 spectrofluorometer (Horiba, Edison, NJ, USA) was used for quantifying fluorescent intensity of ICG, NanoICG, and disassembled NanoICG.

Cytotoxicity

The cytotoxicity of NanoICG and empty NP (self-assembled HA-PBA) were tested using the CCK-8 assay (Dojindo; Rockville, MD). HPNE and KPC cells were seeded in 96-well plates at a density of 25,000 cells/well and allowed to adhere for 24 h. Empty NP and NanoICG were dissolved in DMEM at different concentrations (0, 0.01, 0.05, 0.1 mg/mL) and 200 μL was added to each well. Cells were treated for 24 h and washed twice with PBS. Next, 100 μL of 10% CCK-8 reagent in DMEM was added to each well and incubated at 37 °C. After 50 min, absorbance of each well was measured at 450 nm using a Synergy HTX multi-mode plate reader (BioTek, Winooski, VT, USA). Relative viability was calculated as the absorbance of wells from treated cells divided by the absorbance from wells with untreated cells.

Author Manuscript Author Manuscript Author Manuscript Author Manuscript

Chemotaxis

A chemotaxis assay was adapted from procedures from the National Cancer Institute's Nanotechnology Characterization Laboratory (NCL) (https://ncl.cancer.gov/resources/assay-cascade-protocols): ITA-8. Briefly, HL-60 cells were suspended in serum-free IMDM (SM) and incubated overnight prior to use. 1×10^6 viable cells/mL (as determined by trypan blue) were dispersed onto a MultiScreen filter plate with 3 μm polycarbonate membrane (Merck Millipore, Germany) at 50,000 cells/well. Test samples (150 μL) were added in the feeding tray. The filter plate and feeding tray were gently assembled and incubated for 4 h. After incubation, Calcein AM (CAM) working solution was added to appropriate wells and incubated for 1 h. The solution was then transferred to the optical bottom plate (Thermo Fisher Scientific, Rochester, NY, USA) on a fluorescent plate reader with 485 nm excitation/535 nm emission. Fold increase of chemotaxis was calculated as follows:

$$\text{Background Chemotaxis} = \text{Mean FU}_{\text{SM/CAM}} - \text{Mean FU}_{\text{SM/PBS}}$$
$$\text{Sample Chemotaxis} = \text{Mean FU}_{\text{TS/CAM}} - \text{Mean FU}_{\text{SM/PBS}}$$
$$\text{Fold Increase of Chemotaxis} = \text{Sample Chemotaxis} / \text{Background Chemotaxis}$$

where Mean $FU_{SM/CAM}$ = fluorescence units of HL-60 treated with SM and CAM, Mean $FU_{SM/PBS}$ = fluorescence units of HL-60 treated with SM and PBS, and Mean $FU_{TS/CAM}$ = fluorescence units of HL-60 treated with test samples and CAM.

The theoretical plasma concentration (TPC) of ICG and NanoICG was calculated based on the dose administered to mice below.[23] The calculating formula was adapted from NCL Method ITA-8. TPC of empty NP were based of the mass ratio of HA matrix in NanoICG. The concentrations for 10 × TPC, 1 × TPC, 1/5 × TPC and 1/25 × TPC of ICG were 5.1 μM, 0.51 μM, 0.10 μM, 0.02 μM, respectively; the concentrations for 10 × TPC, 1 × TPC, 1/5 × TPC and 1/25 × TPC of NanoICG were 38 μg/mL, 3.8 μg/mL, 0.76 μg/mL, 0.15 μg/mL, respectively. The same concentrations were used in the phagocytosis assay.

Phagocytosis

Phagocytosis was assessed according to NCL ITA-9. The multi-mode reader and 96-well plate were pre-warmed to 37 °C. HL-60 cell concentration was adjusted to 1×10^7 viable cells/mL (as determined by trypan blue) with complete medium. 100 μL of cell suspension was added per well. 100 μL of controls or test samples were added to pre-warmed wells, followed by 100 μL of luminol working solution (250 μM in PBS). A positive control was prepared by reconstituting zymosan A in PBS with 20% pooled normal human AB serum (Innovative Research, Novi, MI, USA) to a concentration of 2 mg/mL. After mixing, 100 μL of cell suspension was added in sample wells and mixed thoroughly. The kinetic reading process was 1.5 h with 2.1 min reading intervals. The area under the curve (AUC) for each kinetic reading curve from each well was calculated as phagocytic potential.

Tumor model induction

All animal studies were performed under an approved UNMC Institutional Animal Care and Use Committee protocol and procedures were followed in accordance with the institutional guidelines per the Guidelines on the Care and Use of Animals for Scientific Purposes. The

Author Manuscript Author Manuscript Author Manuscript Author Manuscript

guidelines were followed to ensure humane care of the animals. To preclinically evaluate contrast-enhancement of pancreatic cancer by ICG and NanoICG, mature C57BL/6 mice were selected for orthotopic tumor challenge using 10,000 LSL-Kras$^{G12D/+}$;LSL-Trp53$^{R172H/+}$;Pdx-1Cre (KPC)-derived PDAC syngeneic cells per mouse. As described previously,[24] once anesthetized, an approximately 5 mm incision was made into the skin and peritoneum on the abdomen between the hip and rib. This allowed for the spleen to be exteriorized for injection of PBS cell suspension into the body of the pancreas. The peritoneum and skin were then secured using an internal dissolving chromic gut and a 5.0 nylon surgical suture respectively. Animals were warmed, hydrated, and monitored through recovery. Within two weeks of introduction of tumor cells, palpable tumors were detected in all challenged mice.

Near infrared fluorescence imaging

ICG (10 nmol per mouse) or NanoICG (10 nmol ICG per mouse) in 80 μL ultrapure water was intravenously injected into mice via a tail vein (n = 5 mice per group). Mice were euthanized 24 h post injection. Prior to imaging, the liver and spleen were removed to minimize strong ICG fluorescence due to hepatobiliary clearance and to evaluate the ability of ICG and NanoICG to distinguish pancreatic tumor from healthy pancreas. A custom-designed FIGS system was employed to detect contrast enhancement of ICG and NanoICG in the pancreatic tumors. The imaging system utilizes a handheld fiber-coupled spectroscopic unit that excites ICG and collects wavelength-resolved NIR emission (DeltaNu; Laramie, WY, USA). The spectroscopic unit also serves as the excitation source for a real-time widefield imaging system (Spectropath; Atlanta, GA, USA) that merges a NIR channel (800–950 nm) and a visible color channel for spatial orientation of the NIR signal. The overall design and integration of these systems has been previously reported.[25,26] A laser power of 80 mW at 785 nm was used for wavelength-resolved (800–950 nm) and widefield imaging.

After FIGS, all mice were necropsied. The pancreas was removed *en bloc* to preserve the anatomical integrity of the primary, stromal, and healthy tissues for fluorescence imaging and histological sectioning. Dissected organs were imaged on a Pearl Trilogy small animal imaging system (LI-COR Biosciences, Lincoln, NE, USA). The fluorescence intensity of each organ was collected with the 800 nm channel and analyzed by Image Studio Ver. 5.0 software (LI-COR Biosciences, Lincoln, NE, USA). The periphery of each organ was identified free-handed to define the region of interest (ROI). Average pixel intensity was used to calculate signal to noise ratio (SNR), which is defined by average tissue intensity per pixel in an ROI/standard deviation of background ROI. Fluorescence intensity plots of representative pancreases were analyzed with ImageJ 1.49v software (National Institutes of Health, Bethesda, MD, USA). To compare against the spectroscopic analysis of each pancreas that was obtained during surgery, a straight line was drawn longitudinally across the pancreas to include as many acquisition points as possible after whole pancreas imaging. The NIR fluorescence intensity along the line was quantified with the *plot profile* function in ImageJ.

Author Manuscript Author Manuscript Author Manuscript Author Manuscript

Histological analysis

Tumor tissue and organs of metastatic interest were embedded in OCT mounting media gel and were frozen rapidly in liquid nitrogen. Pancreatic tissue was positioned to obtain a maximal footprint for both diseased and healthy pancreases. These samples were cut using Cryostat (Leica Biosciences, Buffalo Grove, IL, USA) at a thickness of 8 μm. Sections from each mouse were stained with hematoxylin and eosin (H&E) or left unstained for NIR fluorescence microscopy. Representative slides were imaged with an IX73 Inverted Microscope with a xenon excitation source and captured with a DP80 Digital Camera and displayed by CellSens Dimension 1.13 software (all from Olympus, Japan). H&E stained slides were visualized and imaged with a bright-field filter, unstained slides were imaged for autofluorescence with a FITC filter cube, and NIR fluorescence with an ICG filter cube. Exposure time of ICG and NanoICG were constant throughout all the samples.

In vivo toxicology

To evaluate the systemic toxicity of NanoICG, 15 mature C57BL/6J mice were divided into vehicle control group, low dose group (equivalent to 10 nmol of ICG per mouse) and high dose group (equivalent to 51.6 nmol of ICG per mouse) (5 mice each group). High dose was calculated based of FDA recommended upper limit dosage of ICG. The mice were treated correspondingly by *i.v.* injection. 72 h after the injection, whole blood was collected into lithium heparin coated blood collection tubes (BD Vacutainer, Franklin Lakes, NJ, USA) and K_2EDTA coated blood collection tubes (BD Microtainer, Franklin Lakes, NJ, USA) by heart puncture. Comprehensive diagnostic profiles of the blood samples were determined by chemistry analyzer (Abaxis, Union City, CA, USA) and complete blood counts were determined by a hematology analyzer (Abaxis, Union City, CA, USA). Livers, lungs, spleens and kidneys were collected, fixed, sectioned and HE-stained for pathological examination.

Statistical analysis

Data was analyzed in Prism 7 software (Graphpad, La Jolla, CA, USA). Cytotoxicity was analyzed using 2-way ANOVA with Tukey's multiple comparisons test; chemotaxis and phagocytosis were analyzed using a 1-way ANOVA and Tukey's multiple comparisons test; biodistribution was analyzed using multiple t tests. *In vivo* toxicity was analyzed with Kruskal-Wallis test. All data is shown as mean ± standard deviation (SD).

Results

Characterization of NanoICG

The mean hydrodynamic diameter, NIRF property, and microscopic morphology of NanoICG are reported in Supplementary Information.

Cytotoxicity

The relative viability of HPNE and KPC cells were calculated by normalizing to untreated cells. Overall, the relative viability of HPNE and KPC cells, which were treated with empty NP and NanoICG, was close to 1. No significant differences were observed between 0.1,

Author Manuscript Author Manuscript Author Manuscript Author Manuscript

0.01 and 0.001 mg/mL (Figure 1). Additionally, no significant difference was detected between empty NP and NanoICG. Empty NP and NanoICG did not impair the metabolic activity of healthy pancreatic epithelial cells.

Chemotaxis

There was a 6.79-fold induction of chemotaxis towards complete medium (positive control) as compared to PBS. In contrast, ICG, NanoICG and empty NP ($p < 0.0001$) showed relative values (as compared to PBS) of 0.63 ± 0.02 for 10 × TPC of ICG, 0.63 ± 0.04 for 10 × TPC of NanoICG and 0.60 ± 0.01 for 10 × TPC of empty NP ($n = 3$) (Figure 2A). The lowest concentration (1/25 × TPC) of ICG, NanoICG and empty NP showed relative chemotaxis induction (as compared to PBS) of 0.85 ± 0.02, 0.87 ± 0.03, and 0.81 ± 0.01 times, respectively ($n = 3$). These results demonstrate that NanoICG and empty NP have no significant chemoattractant properties.

Phagocytosis

HL-60 displayed low phagocytic activity toward PBS, ICG, NanoICG, and empty NP, regardless of test sample concentrations (Figure 2B). In comparison, zymosan A was internalized to a significantly higher extent ($p < 0.0001$), with AUC values 1.87, 1.83 and 1.93 times higher than 10 × TPC for ICG, NanoICG and empty NP, respectively. There was no significant effect of 10 × TPC of ICG, NanoICG and empty NP on phagocytosis as compared to PBS [1.03 ± 0.02, 1.03 ± 0.01 and 1.00 ± 0.01 respectively ($n = 6$)].

Detection of ICG and NanoICG in tumor-bearing mice with IGS

ICG and NanoICG were examined for suitability for IGS as schematically depicted in Figure 3A. Intraoperative imaging demonstrated that NanoICG and ICG could both be detected by IGS in pancreatic tumors; however, NanoICG resulted in more complete and intense enhancement of the tumor when compared to ICG under identical experimental conditions (both were excited with 80 mW power at a constant distance from the tumor) (Figure 3, *bottom*). Spectra collected from these regions are in close agreement with the NIR fluorescence detected in wide-field imaging channel, indicating stronger NIR fluorescence in mice injected with NanoICG (Figure 3, *middle*); at the peak emission wavelength of 814 nm, the fluorescent signal of NanoICG treated pancreatic tumor is 2.03 times of that in ICG group. The IGS images demonstrated an improved contrast profile with NanoICG in orthotopic PDAC detection.

Ex vivo analysis of fluorescence accumulation of pancreatic tumor

NIRF images of the pancreas showed higher accumulation of fluorescent signal in the tumor portion of NanoICG treated pancreas compared with that of ICG, as shown in Figure 4B (4A is a bright field photograph of the pancreas for spatial reference). Figure 4C shows the quantified fluorescence intensity from the spectroscopic pen at acquisition locations across the pancreas to determine the NIR signal and tumor contrast. Spots in the pancreatic tail, which correspond to the location where the KPC PDAC cells were implanted, were brighter compared with the head and body. The point spectroscopic measurements were consistent to whole pancreas NIR images as shown in Figure 4D, where a line was drawn across the

Author Manuscript Author Manuscript Author Manuscript Author Manuscript

pancreas image to obtain as many data points as possible from non- and contrast-enhanced regions, which depicted healthy tissue and PDAC, respectively. The average fluorescent intensities of the healthy and tumor portions of the pancreas were 0.35 ± 0.12 AU and 0.77 ± 0.12 AU, respectively, for ICG. In comparison, the average fluorescence intensity of the healthy and tumor portions were 0.41 ± 0.10 AU and 2.30 ± 0.67 AU, respectively, for NanoICG. The average fold-increases of the tumor portion of the pancreas compared with the healthy portion of the pancreas were 2.20 and 5.61 for ICG and NanoICG, respectively.

During sectioning, the surfaces of the solid tumors were visually observed to be light yellow in color, which is indicative of a high-degree fibrosis.[27] H&E stained tumor slides displayed characteristic poorly differentiated adenocarcinoma with high stroma content (Figure 4E, *left*). Normal pancreatic morphology was shown in a slide from benign pancreatic tissue (Figure 4E, *right*). A higher level of NIRF signal was observed throughout the tumor portion of pancreas treated with NanoICG compared with those treated with ICG (Figure 4E).

The borders of splenic metastasis and healthy spleen tissue were identified by H&E stained slides as shown in Figure 5. Fluorescent signal was detected along the borderline of tumor in the NanoICG treated group but not in the ICG treated group.

Relative biodistribution of ICG and NanoICG in PDAC

The fluorescence intensity of ICG and NanoICG was evaluated among organs harvested from the mice with the orthotopic PDAC model. Overall, higher SNR signal was observed in pancreas in the NanoICG-treated group compared with ICG-treated group with $p < 0.0001$ (Figure 6A). Between organs, significantly higher signals were seen in the liver, spleen, pancreas, bone, heart and lymph node in the NanoICG treated group, which were 5.3, 4.4, 2.1, 2.1, 2.3, 2.2-fold higher compared with ICG treated group respectively. On the other hand, ICG displayed a great propensity to be cleared by the GI tract as determined by semi-quantified NIRF images (Figure 6C), whereas for NanoICG, increased liver and spleen signal, suggestive of RES clearance (Figure 6B).

In vivo toxicology

To make a comparative study on the potential toxic effect of NanoICG on the treated mice, we carried out blood biochemistry and hematology analysis. Figure 7 shows the levels of standard hematological markers, such as white blood cell (WBC), red blood cell (RBC), hemoglobin (HGB), hematocrit (HCT) and platelet (PLT); The WBC is sensitive to the physiological response, the mean value of vehicle control was in the normal range. There is a slight decrease in the number of WBC for NanoICG-treated groups, but this decrease is not significantly different, and close to the anticipated value provided by the animal supplier [50]. All the other parameters in the NanoICG-treated groups appear to be normal compared with the control group, and be within the normal ranges. In addition, we present the biochemistry results of the mice including albumin (ALB), alkaline phosphatase (ALP), alanine aminotransferase (ALT), amylase (AMY), blood urea nitrogen (BUN), total protein (TP) and globulin (GLOB). Fluctuation was observed in ALP, ALT and GLOB for NanoICG-treated group compared with vehicle control, but still remained within the normal

Author Manuscript Author Manuscript Author Manuscript Author Manuscript

ranges; no difference was observed between NanoICG doses or with the vehicle control. The results of blood biochemistry and hematology analysis suggest no obvious toxicity even with upper limit dose of NanoICG.

To further investigate the *in vivo* toxicity of NanoICG, histological analysis of major organs including liver, spleen, lung and kidney were performed 72 h after intravenous administration of different doses of NanoICG, examined by board-certified pathologist (SMC), and the results are shown in Figure 8. The spleens from all animals were normal. This indicates that there was no overall effect on the immune system as there was excellent preservation of the lymphoid white pulp of the spleen. The kidneys showed no evidence of toxicity, either in the glomeruli, tubules, papilla, vessels, or pelvis. Thus, there is no evidence of nephrotoxicity. In the livers, there were occasional animals with focal mononuclear infiltrate (as indicated by the black arrows), but this was not associated with any evidence of necrosis or regeneration. There was no consistent zonal area involved. There was only 1 animal in the vehicle control group with this finding, none in the low dose group, and 2 of the 3 animals in the high dose group had this finding. Thus, this may reflect a low level of hepatotoxicity. However, these results contradict biochemical analysis that had normal levels of ALT and AST for the vehicle control, low dose, and high dose of NanoICG (Figure 7). In the lung, there was 1 animal in the vehicle control group that showed focal consolidation of the alveoli without inflammation, 1 animal in the low dose group that showed focal peribronchiolar chronic inflammation, and 1 animal in the high dose that also showed focal alveolar focal peribronchiolar and alveolar inflammation (as indicated by black arrows). It is most likely that these lung changes reflect the intravenous administration of the material and not related to the material that was injected.

Discussion

The formulation of HA-derived NPs has advantages, most notably overcoming poor aqueous solubility of therapeutic or imaging agents.[28] Second, HA-derived NPs exhibit prolonged circulation and low toxicity to healthy tissues.[29–31] Third, the possibility of tumor targeting, including by specific binding of CD44[32] and through the enhanced permeability and retention (EPR)[28] effect, makes it promising for cancer imaging and therapy. In this study, HA polymers were conjugated with PBA to obtain amphiphilic HA, which readily entrapped amphiphilic ICG in aqueous solution. By incorporating ICG into an HA-derived NP contrast agent, ICG accumulation in tumor was increased (Figure 3, 4 and 6), potentially due to the so-called EPR effect,[28,33] while mitigating potential toxicity from the innate immune system (Figure 2).

Overcoming the immune system barrier is a key step for targeted delivery of contrast agents. Gallagher *et al.* reported that HL-60 cells exhibited responsiveness to chemoattractant and phagocytic activity that were commensurate with the proportion of mature granulocytes.[34] Others have reported that HA species of molecular weights from 792 to 3×10^6 Da all stimulated phagocytic and chemotactic function of polymorphonuclear leukocytes, and, 10 kDa HA was reported as a potent stimulator of the innate immune system.[35,36] However, for HA derived nanosystems, different molecular weight of HA modified liposomes did not cause complement or macrophage activation.[37] In the *in vitro* studies reported here, no

Author Manuscript Author Manuscript Author Manuscript Author Manuscript

significant immunotoxicity was observed except a slight inverse dose-dependency in chemoattractant potential of test samples. The possible explanation is that the volume ratio of SM, a potent chemoattractant for HL-60, increased proportionally as test samples were diluted.

Contrast enhancement within whole pancreas was observed both in ICG and NanoICG treated groups (Figure 4, 6). ICG is a small, amphiphilic dye molecule. After injection, ICG is bound immediately with albumin and other serum proteins and then liberated into liver and cleared out in bile resulting in a half-life of less than 20 min in healthy humans.[33] NIR images of S-180 tumor were reported with obvious contrast 2 h to 48 h post ICG injection, likely from the EPR effect of ICG bound albumin.[33] In Figure 4B, a slight accumulation of ICG was observed in pancreatic tumor, which is comparable to mice with S-180 tumors.[33] In comparison, a more apparent contrast enhancement between healthy and diseased portions of pancreas was observed in NanoICG recipients (Figure 4B). Qhattal and colleagues[38] reported that tumor targeting benefited extensively from long systemic circulation of nanosystems, while Han *et al.*[39] assert that HA performs like PEG by increasing plasma half-life while displaying limited immunotoxicity. Thus, accumulation of NanoICG in tumor could be due to prolonged circulation of HA based nanosystems.

Bouvet *et al.* reported that metastatic lesions of an orthotopic pancreatic cancer model were detected in spleen, bowel, and omentum, as visualized by implanting GFP transfected BxPC-3 cells. By inspecting intravitally, tumor and metastatic area were quantified for growth monitoring.[40] Wang *et al.* reported a dual optical and MR imaging agent, denoted by Cy5.5-ATF-IO, was able to detect intraperitoneal metastatic lesions of PDAC as small as 0.5 mm^3 in optical NIR imaging.[14] Furthermore, optical NIR imaging could detect as little as 1×10^4 tumor cells, which was 1/10 of that which can be detected by MRI.[14] Another study showed that CA19-9 conjugated AlexaFluor488 were potent at detecting micrometastases of PDAC including splenic, peritoneal and liver.[10] In this study, microscopic lesions of splenic metastasis were obviously visualized by NanoICG (Figure 5) and mostly accumulated at the lesion periphery.

An important limitation for targeted delivery of HA-decorated NP is preferential uptake by RES system.[28] On one hand, it has been empirically shown that NPs with size less than 100 nm, neutral or anionic charge, and lower complement binding can avoid RES uptake after *i.v.* administration.[37] Additionally, Qhattal *et al.* found that high molecular weight (HMW) HA grafted liposomes were cleared much faster than low MW HA,[38] because HMW HA had a higher affinity with HARE or LYVE-1, which were widely expressed in normal sinusoidal endothelial cells of the liver, spleen, and activated tissue macrophages.[41] Consequently, NPs that derived with 10 kDa HA could accumulate to a lower degree in liver in that scenario. However, in Figure 6A, NanoICG displayed marked accumulation in liver and spleen ($p < 0.0001$) compared with ICG, which was indicative of increased RES uptake. Further studies are ongoing to determine an optimized HA MW for formulation of NanoICG for pancreatic tumor delivery balanced with minimized RES uptake.

Endogenous HA may play an important role in the biology of pancreatic cancer,[42] as expression of high and low molecular weight forms of HA have been reported to inhibit or

Author Manuscript Author Manuscript Author Manuscript Author Manuscript

enhance malignant properties of pancreatic cancer cells in experimental models. Careful analysis of human samples suggests that HA is expressed by greater than 85% of human pancreatic cancers;[43] however, its expression is not correlated with improved or worse outcome in humans. HA is also the target of therapeutic approaches in which its targeted degradation by PEGylated hyaluronidase is used to improve drug delivery,[44] or alternatively, HA complexes are being developed as drug delivery agents.[45,46] Taken together, our results presented here and the existing and emerging literature strongly support further investigation into the biology and use of HA as delivery vehicle and/or a targeting agent in pancreatic cancer.

In terms of *in vivo* safety, results from healthy C57BL/6J mice after vehicle or one of two NanoICG doses were in concordance with others. For example, HA-derived amphiphilic polymers were reported to demonstrate a protective effect against cisplatin or doxorubicin-induced hepatotoxicity and nephrotoxicity,[47,48] which demonstrates that the self-assembled drug carriers-constructed by HA conjugated hydrophobic moiety-are effective at reducing systemic toxicities. On the other hand, Rao *et al.* reported that HA-derived nanocarriers can control the release of drug payload, depending on the reversible interaction of HA-containing carriers and drugs.[49] This is consistent with the recent results of Hill, *et* al, which showed controlled dye release rate from amphiphilic HA nanostructures.[17] Histologic changes are likely not treatment related as they are minimal, similar to what is seen in controls of this strain both in this study, and, historically, is not associated with necrosis, is not localized to a specific zone of the liver lobule, and is not associated with increased serum enzymes. Accordingly, we hypothesize that negligible toxicity from NanoICG could be due to a combination of several factors: imaging agent was administered with singular and low dose; ICG was entrapped in a stable state through π-π stacking with PBA,[22] which could affect ICG release; and released ICG is an FDA-approved medical diagnostic agent with low inherent toxicity.

NanoICG, an HA-derived NP that physico-chemically entraps ICG, displayed a nontoxic safety profile *in vitro* and *in vivo* and provided significant NIR signal for guidance for intraoperative detection of PDAC *in vivo*. The fluorescence intensity of NanoICG was higher compared to ICG both in pancreas and splenic metastasis, which was confirmed by NIRF imaging, FIGS and microscopic analysis. In conclusion, NanoICG exhibited improved efficacy at detecting pancreatic tumors in an orthotopic pancreatic cancer model with negligible NP-derived toxicity, suggesting that NanoICG is a promising potential contrast agent for guiding pancreatic tumor removal.

Supplementary Material

Refer to Web version on PubMed Central for supplementary material.

Acknowledgments

This work was supported in part by the National Institutes of Health [grant numbers R00CA153916, R01EB019449, P50CA127297, P20 GM103480, U01CA210240, 1S10RR17846, 1S10RR027940, and P30CA036727 (Fred and Pamela Buffett Cancer Center at UNMC)], the Nebraska Cattlemen's Ball Development Fund, and the Nebraska Research Initiative.

Author Manuscript Author Manuscript Author Manuscript Author Manuscript

We thank Thomas C. Caffrey and Kelly A O'Connell for technical support with orthotopic pancreatic cancer model on C57BL/6J mice. We also thank Dr. Michel J. Ouellette for sharing HPNE cell lines. We thank Ms. Lora Arnold for technical guidance for toxicological analysis.

Abbreviations

ATF	amino-terminal fragment
AU	arbitrary unit
CAM	Calcein AM
CCK-8	cell counting kit-8
CT	computed tomography
DMSO	dimethyl sulphoxide
EGF	epidermal growth factor
EPR	enhanced permeability and retention
FIGS	fluorescence image-guided surgery
GI tract	gastrointestinal tract
H&E	hematoxylin and eosin
HA	hyaluronic acid
HMW	high molecular weight
HA-PBA	HA-aminopropyl-1-pyrenebutanamide
HPNE	human pancreatic nestin-expressing epithelial
ICG	indocyanine green
IFSC	intraoperative frozen-section analysis
KPC	LSL-Kras$^{G12D/+}$ LSL-Trp53$^{R172H/+}$ Pdx-1Cre
LMW	low molecular weight
MMP	matrix metalloproteinases
MRI	magnetic resonance imaging
NanoICG	HA-derived nanoparticles with physico-chemically entrapped ICG
NIR	near infrared
NIRF	near infrared fluorescence
PDAC	pancreatic ductal adenocarcinoma

Author Manuscript Author Manuscript Author Manuscript Author Manuscript

PET	positron emission tomography
RES system	reticuloendothelial system
ROI	region of interest
SD	standard deviation
SNR	signal to noise ratio
TPC	theoretical plasma concentration
uPA	urokinase plasminogen activator
US	ultrasonography
WBC	white blood cells
RBC	red blood cells
HGB	hemoglobin
HCT	hematocrit
PLT	platelet
ALB	albumin
ALP	alkaline phosphatase
ALT	alanine aminotransferase
AMY	amylase
BUN	blood urea nitrogen
TP	total protein
GLOB	globulin

References

1. Johnston WC, Hoen HM, Cassera MA, Newell PH, Hammill CW, Hansen PD, et al. Total pancreatectomy for pancreatic ductal adenocarcinoma: review of the National Cancer Data Base. HPB. 2016; 18(1):21–28. [PubMed: 26776847]
2. Cleary SP, Gryfe R, Guindi M, Greig P, Smith L, Mackenzie R, et al. Prognostic factors in resected pancreatic adenocarcinoma: Analysis of actual 5-year survivors1 1No competing interests declared. J Am Coll Surg [Internet]. 2004; 198(5):722–731. Available from: http://linkinghub.elsevier.com/retrieve/pii/S1072751504000390.
3. Manuel H. Pancreatic Cancer. Pancreatic Cancer. 2012:1605–1617.
4. van der Vorst JR. Near-infrared fluorescence imaging of a solitary fibrous tumor of the pancreas using methylene blue. World J Gastrointest Surg [Internet]. 2012; 4(7):180. Available from: https://www.ncbi.nlm.nih.gov/pmc/articles/PMC3420986/.
5. Vahrmeijer AL, Hutteman M, van der Vorst JR, van de Velde CJH, Frangioni JV. Image-guided cancer surgery using near-infrared fluorescence. Nat Rev Clin Oncol [Internet]. 2013; 10(9):507–518. Available from: https://www.nature.com/articles/nrclinonc.2013.123.

Author Manuscript Author Manuscript Author Manuscript Author Manuscript

6. Handgraaf, H., Boonstra, M., Van Erkel, A. Current and future intraoperative imaging strategies to increase radical resection rates in pancreatic cancer surgery; BioMed Res [Internet]. 2014. p. 8Article ID 890230Available from: https://www.hindawi.com/journals/bmri/2014/890230/abs/
7. Nelson DW, Blanchard TH, Causey MW, Homann JF, Brown TA. Examining the accuracy and clinical usefulness of intraoperative frozen section analysis in the management of pancreatic lesions. Am J Surg [Internet]. 2013; 205(5):613–617. Available from: http://www.sciencedirect.com/science/article/pii/S0002961013001165.
8. Trajkovic-Arsic M, Mohajerani P, Sarantopoulos A, Kalideris E, Steiger K, Esposito I, et al. Multimodal Molecular Imaging of Integrin v 3 for In Vivo Detection of Pancreatic Cancer. J Nucl Med [Internet]. 2014; 55(3):446–451. Available from: http://jnm.snmjournals.org/content/55/3/446.short.
9. Quek C-H, Leong KW. Near-Infrared Fluorescent Nanoprobes for in Vivo Optical Imaging. Nanomaterials [Internet]. 2012; 2(4):92–112. Available from: http://www.mdpi.com/2079-4991/2/2/92/htm.
10. McElroy M, Kaushal S, Luiken GA, Talamini MA, Moossa AR, Hoffman RM, et al. Imaging of primary and metastatic pancreatic cancer using a fluorophore-conjugated anti-CA19-9 antibody for surgical navigation. World J Surg [Internet]. 2008; 32(6):1057–1066. Available from: http://link.springer.com/article/10.1007/s00268-007-9452-1.
11. Frangioni JV. In vivo near-infrared fluorescence imaging. Curr Opin Chem Biol [Internet]. 2003; 7(5):626–34. Available from: http://www.sciencedirect.com/science/article/pii/S1367593103001091.
12. Welsher K, Sherlock SP, Dai H. Deep-tissue anatomical imaging of mice using carbon nanotube fluorophores in the second near-infrared window. Proc Natl Acad Sci [Internet]. 2011; 108(22): 8943–8948. Available from: http://www.pnas.org/content/108/22/8943.short.
13. Metildi CA, Felsen CN, Savariar EN, Nguyen QT, Kaushal S, Hoffman RM, et al. Ratiometric Activatable Cell-Penetrating Peptides Label Pancreatic Cancer, Enabling Fluorescence-Guided Surgery, Which Reduces Metastases and Recurrence in Orthotopic Mouse Models. Ann Surg Oncol [Internet]. 2015; 22(6):2082–2087. Available from: http://link.springer.com/article/10.1245/s10434-014-4144-1.
14. Yang L, Mao H, Cao Z, Wang YA, Peng X, Wang X, et al. Molecular Imaging of Pancreatic Cancer in an Animal Model Using Targeted Multifunctional Nanoparticles. Gastroenterology [Internet]. 2009; 136(5):1514–1525.e2. Available from: http://www.sciencedirect.com/science/article/pii/S0016508509000122.
15. Kosaka N, Ogawa M, Choyke PL, Karassina N, Corona C, McDougall M, et al. In vivo stable tumor-specific painting in various colors using dehalogenase-based protein-tag fluorescent ligands. Bioconjug Chem [Internet]. 2009; 20(7):1367–1374. Available from: http://pubs.acs.org/doi/abs/10.1021/bc9001344.
16. Ogawa M, Kosaka N, Choyke PL, Kobayashi H. In vivo Molecular Imaging of Cancer with a Quenching Near-Infrared Fluorescent Probe Using Conjugates of Monoclonal Antibodies and Indocyanine Green. Cancer Res [Internet]. 2009; 69(4):1268–1272. Available from: http://cancerres.aacrjournals.org/content/69/4/1268.short.
17. Hill T, Kelkar S, Wojtynek N, Souchek J. Near Infrared Fluorescent Nanoparticles Derived from Hyaluronic Acid Improve Tumor Contrast for Image-Guided Surgery. Theranostics [Internet]. 2016; 6(13):2314–2328. Available from: https://www.ncbi.nlm.nih.gov/pmc/articles/PMC5118597/.
18. Ishizawa, T., Fukushima, N., Shibahara, J., Masuda, K. Real-Time Identification of Liver Cancers by Using Indocyanine Green Fluorescent Imaging. Cancer [Internet]. 2009. Available from: http://onlinelibrary.wiley.com/doi/10.1002/cncr.24291/full
19. Solis, MA., Chen, YH., Wong, TY., Bittencourt, VZ., Lin, YC., Huang, LLH. Hyaluronan regulates cell behavior: A potential niche matrix for stem cells [Internet]. Biochem Res Int. 2012. Available from: https://www.hindawi.com/journals/bri/2012/346972/abs/
20. Paul Bulpitt DA. New strategy for chemical modification of hyaluronic acid: Preparation of functionalized derivatives and their use in the formation of novel biocompatible hydrogels. J Biomed Mater Res. 1999; 47(2):152–169. [PubMed: 10449626]

Author Manuscript Author Manuscript Author Manuscript Author Manuscript

21. Prestwich GD, Marecak DM, Marecek JF, Vercruysse KP, Ziebell MR. Controlled chemical modification of hyaluronic acid: synthesis, applications, and biodegradation of hydrazide derivatives. J Control Release. 1998; 53(1–3):93–103. [PubMed: 9741917]
22. Hill TK, Abdulahad A, Kelkar SS, Marini FC, Long TE, Provenzale JM, et al. Indocyanine green-loaded nanoparticles for image-guided tumor surgery. Bioconjug Chem [Internet]. 2015; 26(2): 294–303. Available from: http://pubs.acs.org/doi/abs/10.1021/bc5005679.
23. Dobrovolskaia MA, McNeil SE. Understanding the correlation between in vitro and in vivo immunotoxicity tests for nanomedicines. J Control Release [Internet]. 2013; 172(2):456–466. Available from: http://www.sciencedirect.com/science/article/pii/S0168365913003155.
24. Tsutsumida H. RNA Interference Suppression of MUC1 Reduces the Growth Rate and Metastatic Phenotype of Human Pancreatic Cancer Cells. Clin Cancer Res [Internet]. 2006; 12(10):2976–2987. Available from: http://clincancerres.aacrjournals.org/content/12/10/2976.short.
25. Mohs AM, Mancini MC, Singhal S, Provenzale JM, Leyland-Jones B, Wang MD, et al. Hand-held spectroscopic device for in vivo and intraoperative tumor detection: Contrast enhancement, detection sensitivity, and tissue penetration. Anal Chem [Internet]. 2010; 82(21):9058–9065. Available from: http://pubs.acs.org/doi/abs/10.1021/ac102058k.
26. Mohs A, Mancini M, Provenzale J, Saba CF, Cornell KK, Howerth EW, et al. An integrated widefield imaging and spectroscopy system for contrast enhanced, image-guided research of tumors. IEEE Trans Biomed Eng. 2015; 62(5):1416–1424. [PubMed: 25585410]
27. Chung EM, Travis MD, Conran RM. Pancreatic Tumors in Children: Radiologic-Pathologic Correlation. RadioGraphics [Internet]. 2006; 26(4):1211–1238. Available from: http://pubs.rsna.org/doi/abs/10.1148/rg.264065012.
28. Dosio F, Arpicco S, Stella B, Fattal E. Hyaluronic acid for anticancer drug and nucleic acid delivery. Adv Drug Deliv Rev [Internet]. 2015; 97:204–236. Available from: http://www.sciencedirect.com/science/article/pii/S0169409X15002756.
29. Water JJ, Kim Y, Maltesen MJ, Franzyk H, Foged C, Nielsen HM. Hyaluronic acid-based nanoge ls produced by microfluidics-facilitated self-assembly improves the safety profile of the cationic host defense peptide novicidin. Pharm Res [Internet]. 2015; 32(8):2727–2735. Available from: http://link.springer.com/article/10.1007/s11095-015-1658-6.
30. Huang J, Zhang H, Yu Y, Chen Y, Wang D, Zhang G, et al. Biodegradable self-assembled nanoparticles of poly (d,l-lactide-co-glycolide)/hyaluronic acid block copolymers for target delivery of docetaxel to breast cancer. Biomaterials [Internet]. 2014; 35(1):550–566. Available from: http://www.sciencedirect.com/science/article/pii/S0142961213011897.
31. Liu Y, Sun J, Zhang P, He Z. Amphiphilic polysaccharide-hydrophobicized graft polymeric micelles for drug delivery nanosystems. Curr Med Chem [Internet]. 2011; 18(17):2638–48. Available from: http://www.ingentaconnect.com/content/ben/cmc/2011/00000018/00000017/art00012.
32. Misra S, Heldin P, Hase S, Karamanos NK, Skandalis SS, Markwald RR, et al. Hyaluronan-CD44 iteractions as potential targets for cancer therapy. FEBS J. 2011; 278:1429–1443. [PubMed: 21362138]
33. Maeda H, Nakamura H, Fang J. The EPR effect for macromolecular drug delivery to solid tumors: Improvement of tumor uptake, lowering of systemic toxicity, and distinct tumor imaging in vivo. Adv Drug Deliv Rev [Internet]. 2013; 65(1):71–79. Available from: http://www.sciencedirect.com/science/article/pii/S0169409X12003201.
34. Gallagher R, Collins S, Trujillo J, McCredie K, Ahearn M, Tsai S, et al. Characterization of the continuous, differentiating myeloid cell line (HL-60) from a patient with acute promyelocytic leukemia. Blood. 1979; 54(3):713–733. [PubMed: 288488]
35. McKee CM, Penno MB, Cowman M, Burdick MD, Strieter RM, Bao C, et al. Hyaluronan (HA) fragments induce chemokine gene expression in alveolar macrophages: The role of HA size and CD44. J Clin Invest [Internet]. 1996; 98(10):2403–2413. Available from: https://www.ncbi.nlm.nih.gov/pmc/articles/PMC507693/.
36. Termeer CC, Hennies J, Voith U, Ahrens TM, Weiss J, Prehm P, et al. Oligosaccharides of Hyaluronan Are Potent Activators of Dendritic Cells. J Immunol [Internet]. 2000; 165(4):1863–1870. Available from: http://www.jimmunol.org/content/165/4/1863.short.

Author Manuscript Author Manuscript Author Manuscript Author Manuscript

37. Peer D, Margalit R. Loading mitomycin C inside long circulating hyaluronan targeted nano-liposomes increases its antitumor activity in three mice tumor models. Int J Cancer [Internet]. 2004; 108(5):780–789. Available from: http://onlinelibrary.wiley.com/doi/10.1002/ijc.11615/full.
38. Qhattal S, Hye T, Alali A, Liu X. Hyaluronan Polymer Length, Grafting Density, and Surface Poly (ethylene glycol) Coating Influence in Vivo Circulation and Tumor Targeting of Hyaluronan-grafted liposomes. ACS Nano. 2015; 8(6):5423–5440.
39. Han X, Li Z, Sun J, Luo C, Li L, Liu Y, et al. Stealth CD44-targeted hyaluronic acid supramolecular nanoassemblies for doxorubicin delivery: Probing the effect of uncovalent pegylation degree on cellular uptake and blood long circulation. J Control Release [Internet]. 2015; 197:29–40. Available from: http://www.sciencedirect.com/science/article/pii/S0168365914007275.
40. Bouvet M, Wang J, Nardin SR, Nassirpour R, Yang M, Baranov E, et al. Real-Time optical imaging of primary tumor growth and multiple metastatic events in a pancreatic cancer orthotopic model. Cancer Res. 2002; 62(5):1534–1540. [PubMed: 11888932]
41. Ruoslahti E, Bhatia SN, Sailor MJ. Targeting of drugs and nanoparticles to tumors. J Cell Biol [Internet]. 2010; 188(6):759–768. Available from: http://jcb.rupress.org/content/188/6/759.short.
42. Sato N, Kohi S, Hirata K, Goggins M. Role of hyaluronan in pancreatic cancer biology and therapy: Once again in the spotlight [Internet]. Cancer Sci. 2016; 107(5):569–575. Available from: http://onlinelibrary.wiley.com/doi/10.1111/cas.12913/full. [PubMed: 26918382]
43. Gebauer F, Kemper M, Sauter G, Prehm P, Schumacher U. Is hyaluronan deposition in the stroma of pancreatic ductal adenocarcinoma of prognostic significance? PLoS One. 2017; 12(6):e0178703. [PubMed: 28582436]
44. Wong KM, Horton KJ, Coveler AL, Hingorani SR, Harris WP. Targeting the Tumor Stroma: the Biology and Clinical Development of Pegylated Recombinant Human Hyaluronidase (PEGPH20). Curr Oncol Rep [Internet]. 2017; 19(7):47. Available from: https://www.ncbi.nlm.nih.gov/pubmed/28589527.
45. Kim J, Park Y. Improved Antitumor Efficacy of Hyaluronic Acid-Complexed Paclitaxel Nanoemulsions in Treating Non-Small Cell Lung Cancer. Biomol Ther (Seoul). 2017; 25(4):411–416. [PubMed: 28208014]
46. Lu Z, Su J, Li Z, Zhan Y, Ye D. Hyaluronic acid-coated, prodrug-based nanostructured lipid carriers for enhanced pancreatic cancer therapy. Drug Dev Ind Pharm [Internet]. 2017; 43(1):160–170. Available from: https://www.tandfonline.com/doi/full/10.1080/03639045.2016.1226337.
47. Hyaluronic acid-green tea catechin micellar nanocomplexes: Fail-safe cisplatin nanomedicine for the treatment of ovarian cancer without off-target toxicity. Biomaterials [Internet]. 2017; 148:41–53. Available from: http://www.sciencedirect.com/science/article/pii/S0142961217306129#fig1.
48. Wang J, Ma W, Guo Q, Li Y, Hu Z, Zhu Z, et al. The effect of dual-functional hyaluronic acid-vitamin E succinate micelles on targeting delivery of doxorubicin. Int J Nanomedicine [Internet]. 2016; 11:5851–5870. Available from: http://www.ncbi.nlm.nih.gov/pubmed/27853369.
49. Rao NV, Yoon HY, Han HS, Ko H, Son S, Lee M, et al. Recent developments in hyaluronic acid-based nanomedicine for targeted cancer treatment. Expert Opin Drug Deliv [Internet]. 2016; 13(2): 239–252. Available from: http://www.ncbi.nlm.nih.gov/pubmed/26653872.
50. Reference ranges of hematology data of healthy female C57BL/6J mcie were obtained from Jackson Laboratory (updated in December 2007): http://jackson.jax.org/rs/444-BUH-304/images/physiological_data_000664.pdf

Author Manuscript Author Manuscript Author Manuscript Author Manuscript

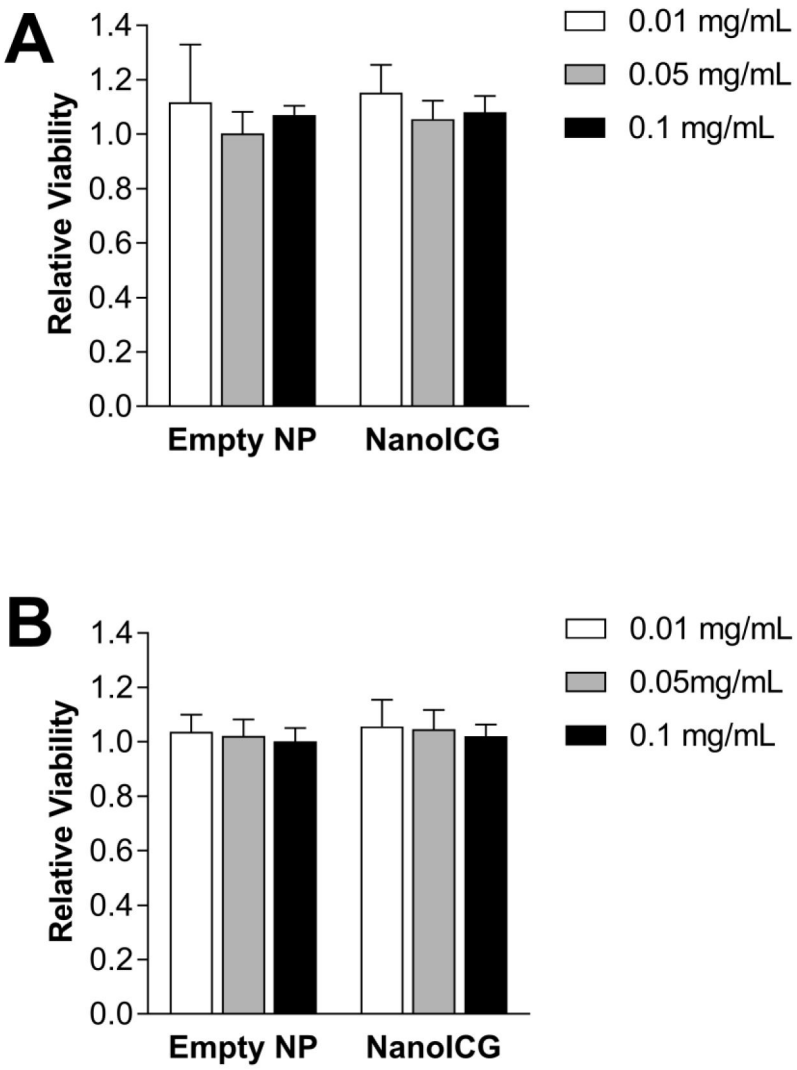

Figure 1.

CCK-8 assay was performed on (A) HPNE cells and (B) KPC cells treated with variable concentrations of empty NP and NanoICG for 24 h, $n = 5$, no significant differences were detected between each group.

Author Manuscript Author Manuscript Author Manuscript Author Manuscript

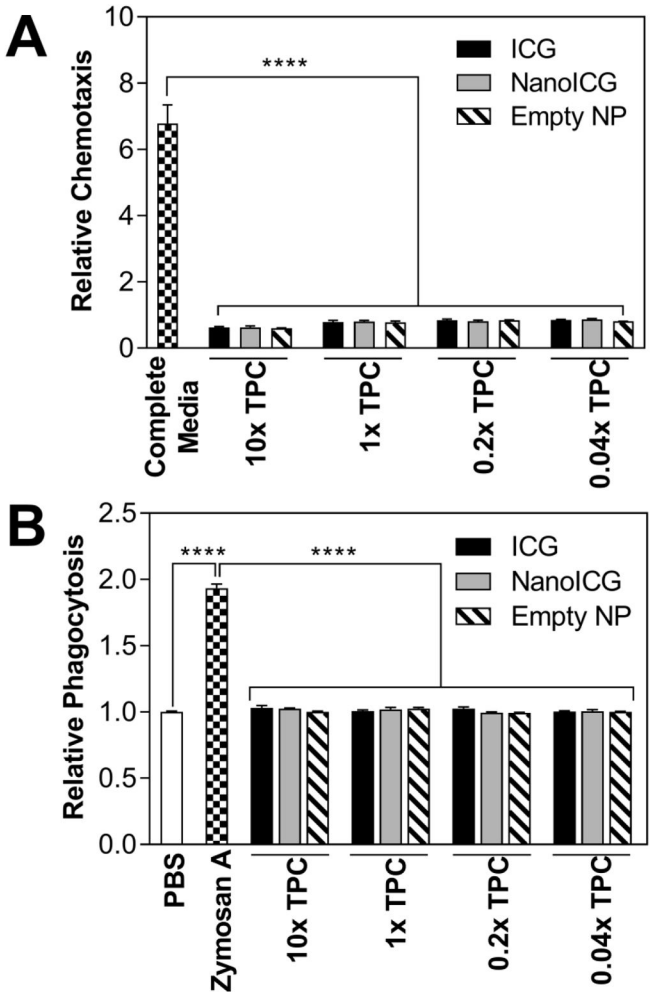

Figure 2.

(A) Chemotaxis assay of HL-60 with ICG, NanoICG and empty NP at varied concentrations based of theoretical plasma concentration (TPC) at 4 h time point. Complete medium is IMDM with 20% FBS. Fluorescent spectra of calcein AM was collected at 485 nm excitation/535 nm emission; (B) Phagocytic assay of NanoICG in HL-60. Zymosan A served as the positive control while PBS was the negative control. Luminesance reading was monitored for 1.5 h with 2.1 min intervals and AUC of fluorescent signal was quantified as chemotactic response. ****$p < 0.0001$.

Author Manuscript Author Manuscript Author Manuscript Author Manuscript

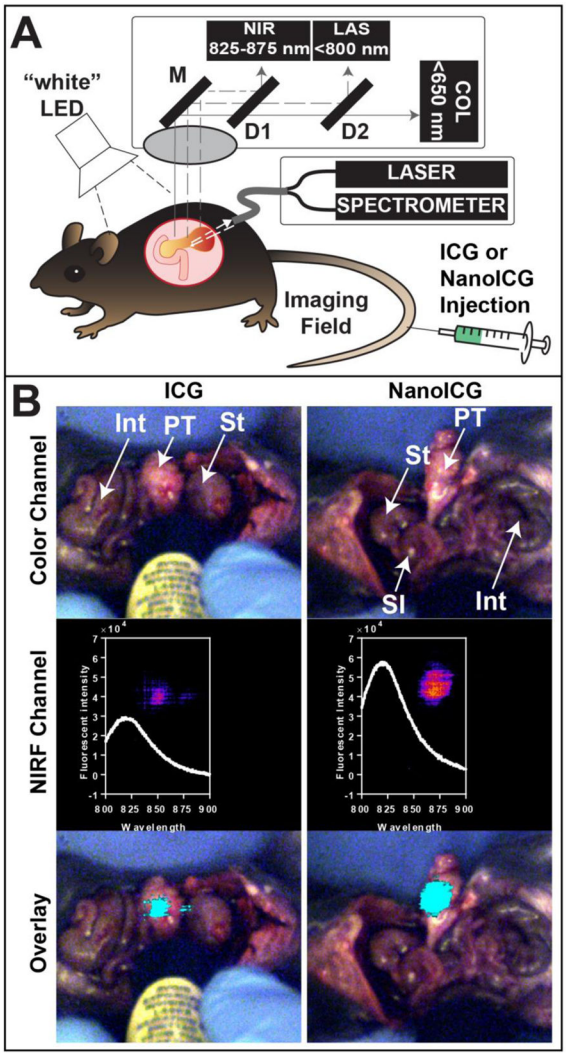

Figure 3.

(A) Schematic of the image-guided surgery system utilized to detect orthotopic PDAC. As described in the text, the system utilizes both wavelength-resolved NIR spectroscopic measurements and a wide-field, multi-detector video camera for real-time surgical guidance that uses the hand-held spectroscopic pen as an excitation source. (B) Images from surgical navigation of pancreatic tumor contrast-enhanced with ICG (*left*) or NanoICG (*right*) 24 h post *i.v.* injection. Livers and spleens were removed due to high background signal from ICG clearance. Int = large intestine, PT = pancreatic tumor, St = stomach, SI = small intestine; (*Top*) Color images show orthotopic PDAC and the location of the handheld spectroscopic pen, which provides NIR spectral information and serves as an excitation source for a widefield imaging system. (*Middle*) Pseudo-colored signal in the NIR channel of the widefield imaging system and the spectroscopic signal from within the contrast-enhanced region; (*Bottom*) NIR signal overlaid (cyan) onto the color image shows robust enhancement of syngeneic, orthotopic pancreatic cancer. Contrast enhancement can be observed with both ICG and NanoICG, with NanoICG having stronger signal (see inset middle row).

Author Manuscript Author Manuscript Author Manuscript Author Manuscript

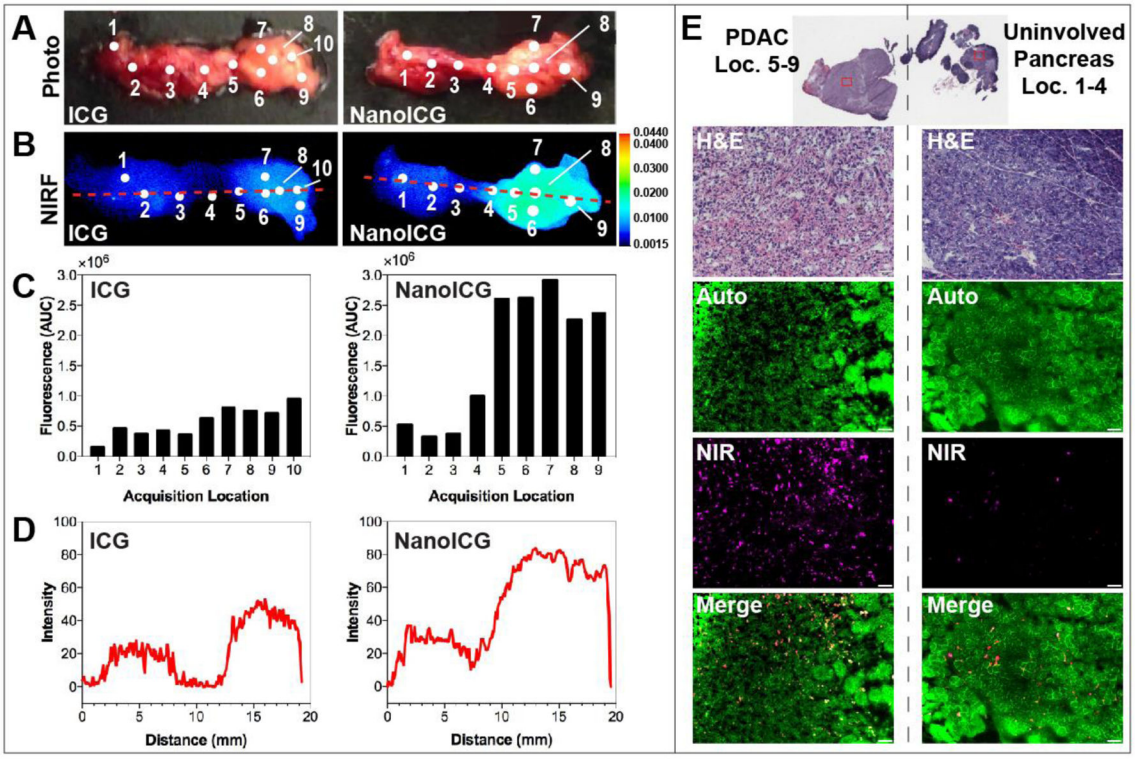

Figure 4.

Ex vivo analysis of ICG and NanoICG accumulation in pancreatic tumor. (A) Photo images and (B) NIRF images of a representative pancreatic tumor marked with acquisition locations of the spectroscopic semi-quantification shown in (B); (C) Fluorescence intensity excited with medium laser power and 1 s integration by the spectroscopic pen component of FIGS system; (D) Plots of intensity values along the red dashed line from the NIRF images quantified by ImageJ; (E) Morphological examination (H&E) and fluorescent signal accumulation (NIR) under microscope of tumor-bearing cancerous pancreas (*left*) and healthy pancreas (*right*) administered with NanoICG. Autofluorescence (Auto) was detected with FITC filter cube which pseudo-colored green, NIR fluorescence was detected with ICG filter cube which pseudo-colored magenta. Scale bar represents 50 μm.

Author Manuscript Author Manuscript Author Manuscript Author Manuscript

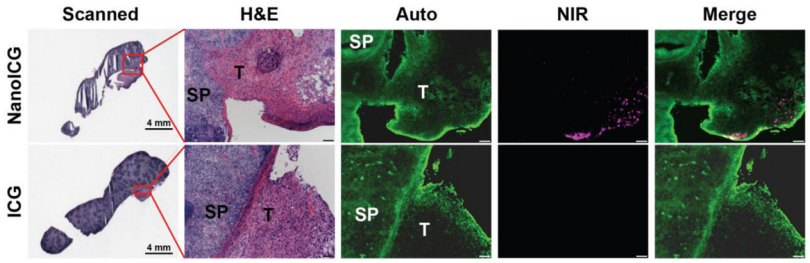

Figure 5.

Histological examination of splenic metastasis of PDAC. Splenic metastasis of PDAC administered with NanoICG (Top) and ICG (Bottom). SP = spleen, T = tumor. Scale bars in panels of H&E, Auto, NIR and Merge represent 100 μm.

Author Manuscript Author Manuscript Author Manuscript Author Manuscript

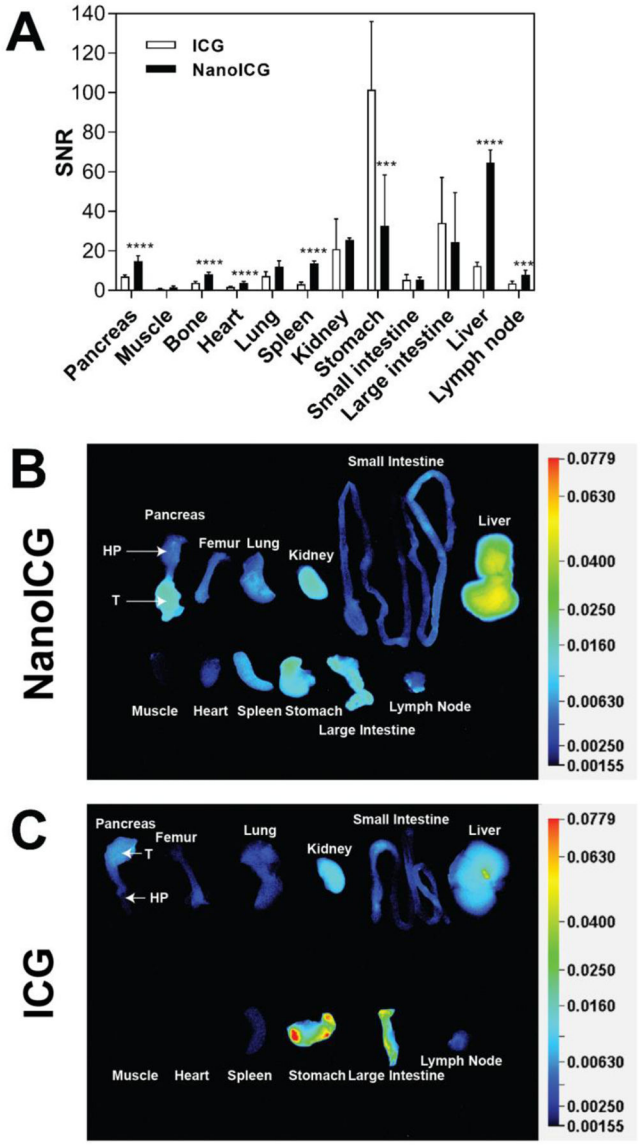

Figure 6.

Quantification of biodistribution of ICG and NanoICG in PDAC mice based on NIRF images at 24 h post contrast agent administration. (A) Quantified distribution of ICG and NanoICG in PDAC mice, $n = 5$, ***$p < 0.001$, ****$p < 0.0001$; (B) Representative NIRF image of indicated necropsied organs from PDAC mice treated with NanoICG; T = tumor, HP = healthy portion; (C) Representative NIRF image of necropsied organs from PDAC mice treated with ICG.

Author Manuscript Author Manuscript Author Manuscript Author Manuscript

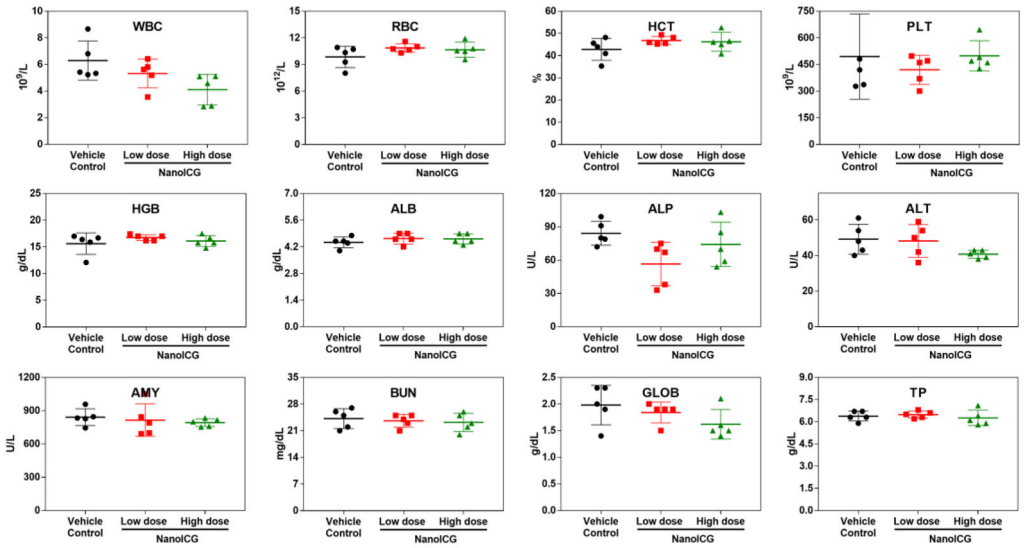

Figure 7.

Hematology results and blood biochemistry results of the vehicle (black), low dose (0.39 mg/kg ICG equivalent, red) and high dose (2 mg/kg ICG equivalent, green) of NanoICG treated mice 72 h after intravenous injection. The results show mean and standard deviation of white blood cells (WBC), red blood cells (RBC), hemoglobin (HGB), hematocrit (HCT), platelet (PLT), albumin (ALB), alkaline phosphatase (ALP), alanine aminotransferase (ALT), amylase (AMY), blood urea nitrogen (BUN), total protein (TP), globulin (GLOB). *N* = 5.

Author Manuscript Author Manuscript Author Manuscript Author Manuscript

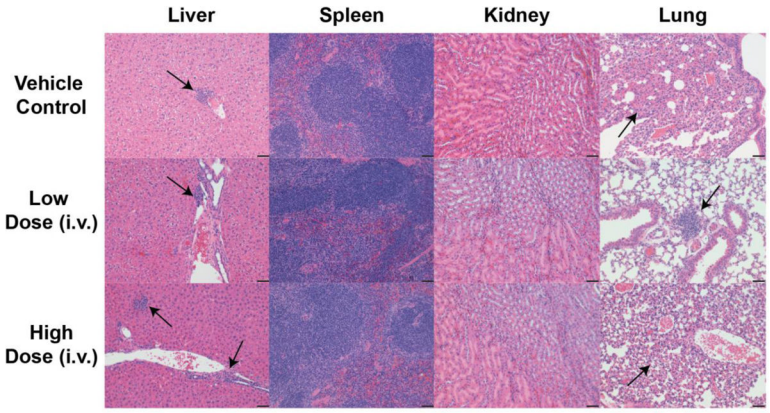

Figure 8.

H&E stained tissue slides (liver, spleen, kidney and lung) of C57BL/6 mice 72 after intravenous injection of vehicle (*top row*), low dose NanoICG (0.39 mg/kg ICG equivalent, *middle row*) and high dose NanoICG (2 mg/kg ICG equivalent, *bottom row*). Black arrows in livers indicated focal mononuclear infiltrate, black arrows in lungs indicated focal consolidation or focal peribronchiolar chronic inflammation. Black bars represent 50 μm, N = 4 for vehicle control, N = 3 for low dose and high dose groups.